Electronic Supporting Information

Liquid metal-created macroporous composite hydrogels with self-healing ability and multiple sensations as artificial flexible sensors

Zhixing Zhang [a], Lin Tang [a], Can Chen [a], Huitao Yu [a], Huihui Bai [a], Ling Wang [a], Mengmeng Qin [a], Yiyu Feng [a, b, c], and Wei Feng [a, b, c]*

a School of Materials Science and Engineering, Tianjin University, Tianjin 300072, P. R. China.

b Key Laboratory of Advanced Ceramics and Machining Technology, Ministry of Education, Tianjin 300072, P. R. China;

c Tianjin Key Laboratory of Composite and Functional Materials, Tianjin 300072, P. R. China;

Corresponding author:

*E-mail: weifeng@tju.edu.cn (W. Feng)

Experimental Section

***Materials*:** Hydrogen peroxide (H_2O_2), hydrochloric acid (HCl), potassium permanganate ($KMnO_4$), ammonium persulfate (APS), and sulfuric acid (H_2SO_4) were purchased from Jiangtian Chemical Technology Co. Ltd. (Tianjin, China). Natural flake graphite (325 mesh) was supplied by Qingdao Meilikun Co. Ltd. (Qingdao, China). Gallium (Ga), and acrylic acid (AA) were purchased from J&K Co. Ltd.

***Synthesis of GO*:** A modified Hummers method was used to synthesize GO.[1] Briefly, $KMnO_4$ (10 g) was added into a mixture of graphite flakes (2 g) and H_2SO_4 (80 mL), followed by stirring for 1.5 h in an ice bath. Subsequently, the vessel was transferred into a water bath, and stirring was continued for another 6 h to complete the deep oxidation process. Next, deionized water (400 mL) was added, followed by uniform stirring. Then, H_2O_2 (10 mL, 30%) was added into the resulting mixture, followed by centrifugation to remove the residual graphite. Finally, a pure GO aqueous solution was obtained.

***Preparation of PAA-LM/rGO Composite Hydrogels*:** PAA-LM/rGO composite hydrogels were synthesized as follows. First, a certain volume of Ga LM was added to a 10 mL aqueous solution of GO (4 mg mL^{-1}). Subsequently, the GO/Ga mixture solution was prepared via sonication for 5 min performed using a probe sonicator (TL-250Y, Jiangsu Tianling Ltd.). Then, the precursor containing AA (1.5 g), APS (20 mg), and water (1 mL) was added. The resulting solution was injected into a silicone mold and subsequently incubated at room temperature (approximately 25 °C) for 24 h. Based on this method, hydrogels with 10, 20, 30, and 40 μL of Ga LM were fabricated and denoted as PAA-LM10/rGO-25, PAA-LM20/rGO-25, PAA-LM30/rGO-25, and PAA-LM40/rGO-25, respectively. For hydrogels synthesized at other temperatures, the samples were denoted as PAA-LM*x*/rGO-*y*, where *x* is the volume of Ga and *y* is the temperature. For example, PAA-LM20/rGO-40 represents the PAA-LM20/rGO hydrogel synthesized at 40 °C.

***Control Experiment*:** A typical PAA-LM hydrogel was prepared. Briefly, Ga (20 μL) was dispersed in water (10 mL) by ultrasonication, and the same precursor was subsequently added. After the reaction, the PAA-LM hydrogel was obtained. Similarly, a pure PAA solution of the same concentration was prepared at 70 °C.

***Confirmation Experiment*:** To confirm H^+ assisted LM reduction of GO, a series of experiments were performed. HCl was used to create an acidic environment. In brief, the GO/Ga mixture solutions containing different mass ratios of LM/GO (1:1, 2:1, and 3:1) were prepared via probe sonication. Afterward, the pH value was adjusted to 2, and these solutions, with adjusted pH, were then stored at room temperature for 24 h. To remove excess LMs, some additional HCl was added into the aforementioned solutions. Finally, the resulting rGO was collected after filtration, and subsequently washed and freeze-dried.

***General Characterization*:** Attenuated total reflectance-Fourier transform infrared (ATR-FTIR) spectroscopy was performed using a Nicolet iS10 spectrometer in the range of 4000–500 cm^{-1} at a resolution of 4 cm^{-1}. X-ray photoelectron spectroscopy (XPS) was performed using an EscaLab 250Xi spectrometer. The X-ray diffraction (XRD) patterns were collected using a Bruker D8 diffractometer with a graphite-filtered Cu-Ka source at a wavelength of 0.154 nm, scanning rate of 8° min^{-1}, voltage of 40 kV, and current of 40 mA. Raman spectroscopy was conducted using a Raman spectrometer with a λ= 514 nm laser (Thermo Electron, DXR Microscope). A scanning electron microscope (SEM, Hitachi S4800, Japan) equipped with energy-dispersive X-ray spectroscopy capabilities was employed to examine the morphologies and compositions of the samples. The thermal stability was measured by thermogravimetric analysis (TGA, Q600 SDT) under nitrogen flow from 30 to 800 °C at a heating rate of 10 °C min^{-1}. The optical microscope (Nikon SMZ745T, Japan) was employed to observe the macroporous structure of hydrogels.

***Porosity Measurement*:** For porosity measurement, various hydrogels were prepared at different temperatures. Notably, the hydrogels obtained at 5 °C were used as reference

hydrogels to calculate the density of the PAA-LM/rGO hydrogels, scince they possessed few or no pores. The porosity factors of these hydrogels were calculated according to the following equations:

$$\rho_G V_G + \rho_{RH} V_H = M_{PH} \tag{1}$$

$$V_G + V_H = V_{PH} \tag{2}$$

$$Porosity\ factor = \frac{V_G}{V_{PH}} \tag{3}$$

where ρ_G is the density of gas, and ρ_{RH} is the density of reference hydrogel, which can be obtained by measuring its volume and mass. V_G and V_H are the volumes of air and pure hydrogel in the porous hydrogel, respectively. V_{PH} and M_{PH} are the volume and mass of the porous hydrogel, respectively. It should be noted that the hydrogel sample was cylindrical in shape, and its total volume and mass could be measured easily. Moreover, when the porous hydrogel is exposed to air, the gas in the hole changes from hydrogen to a mixture of air and hydrogen. However, since the density of gas is much lower than that of hydrogel (air: $\rho_A = 1.29\times10^{-3}$ g/cm^3, hydrogen: $\rho_{H2} = 8.9\times10^{-5}$ g/cm^3, $\rho_{RH} = 1.18$ g/cm^3), the influence of ρ_A or ρ_{H2} on the calculation results is very small. In this study, ρ_A was used to calculate porosity.

***Mechanical Test*:** Tensile and compression tests were performed using a universal mechanical tester (UTM2203, Shenzhen SUNS Technology Stock Co., Ltd.). Rectangular-shaped (10 × 2 × 30 mm) and cylindrical-shaped (15 mm in diameter and 20 mm in height) samples were used for tensile and compression tests, respectively. The test speeds for tensile and compression tests were set at 20 mm/min.

***Self-healing Property*:** Strip-like specimens (10 × 2 × 30 mm) were cut into halves, the two separate halves were then brought into contact without applying stress and stored in a sealed vessel. After self-healing process, a tensile test was performed to evaluate the tensile self-healing efficiency, which is defined as the tensile strength or elongation at break ratio between

the healed sample and the original sample. Similarly, the electrical healed efficiency is defined as the resistance ratio between the healed sample and original sample.

***Electrical Response Measurement*:** Electric measurements were conducted using a TH2830 meter analyzer. The conductivity of the sample was calculated by formula: $k = \frac{l}{R \cdot S}$ (where k is the electrical conductivity; l and S were the length and cross-sectional area of the sample between two electrodes, respectively; R was measured resistance.). For both the capacitance and resistance measurements, copper foils were used as conductive wires to connect the hydrogel system, and the specific measurement method was employed according to the schematic diagram of the corresponding tested item.

Supporting Figures and Tables:

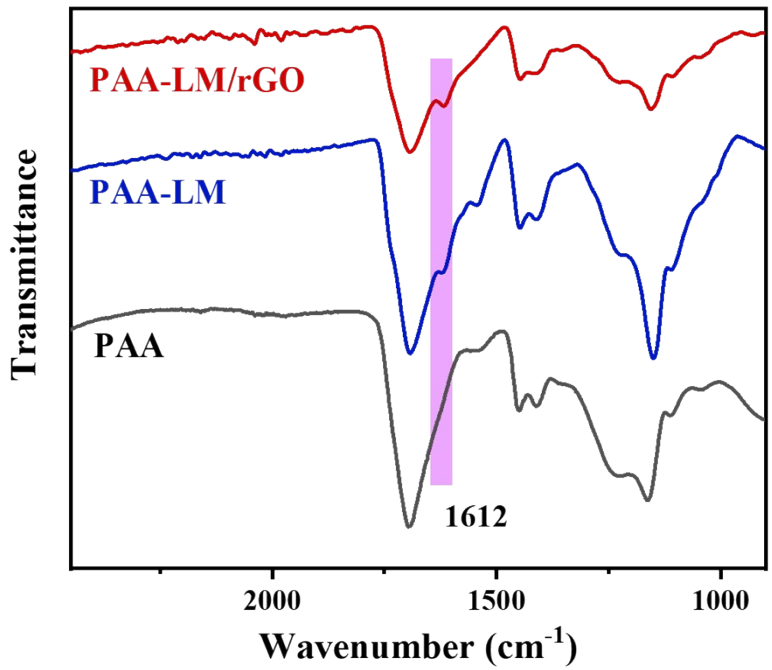

Fig. S1. ATR-FTIR spectra of PAA, PAA-LM and PAA-LM/rGO dry gels.

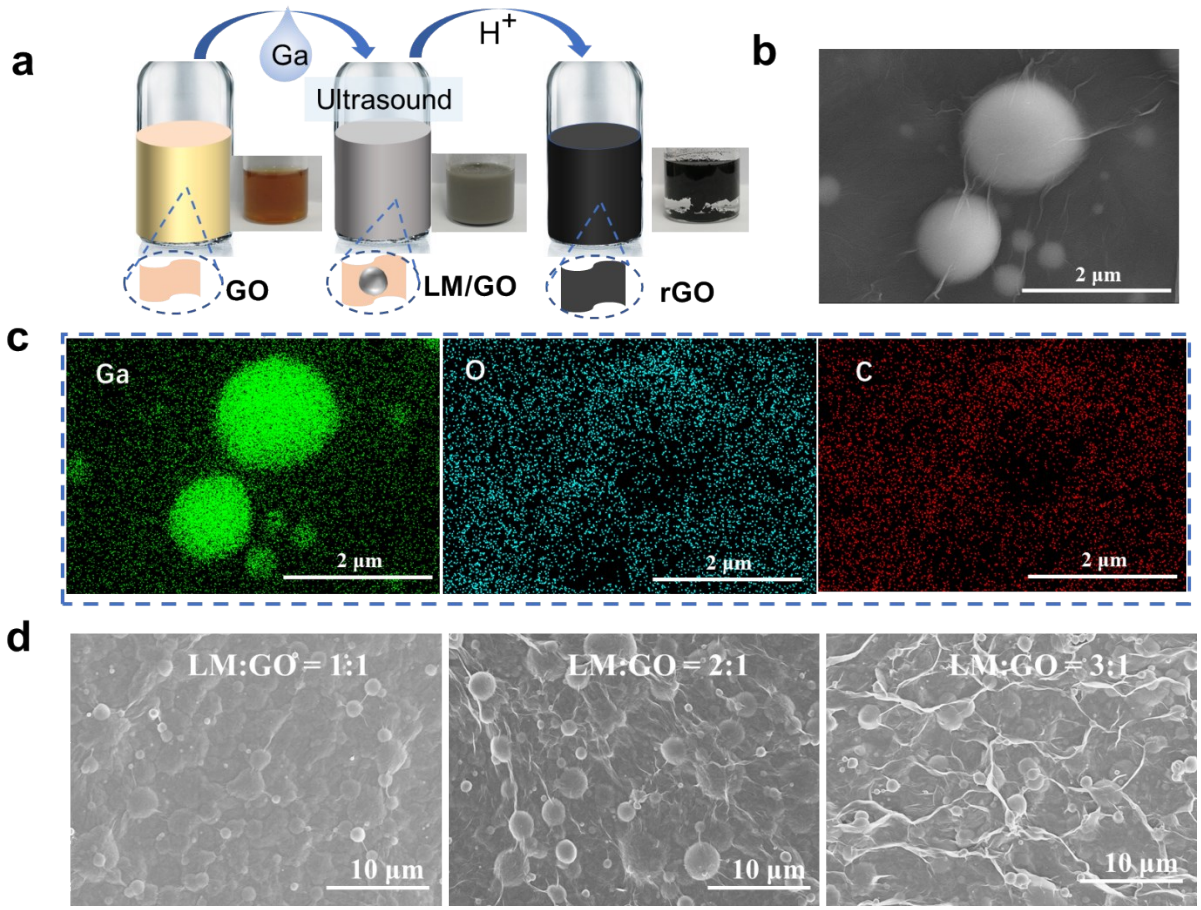

Fig. S2. a) Schematic of LM reduction of GO. b, c) SEM images of LM/GO and the corresponding map sweeping spectrum showing the elemental distribution of Ga, O, and C. d) SEM images of LM/GO hybrid with different weight ratios.

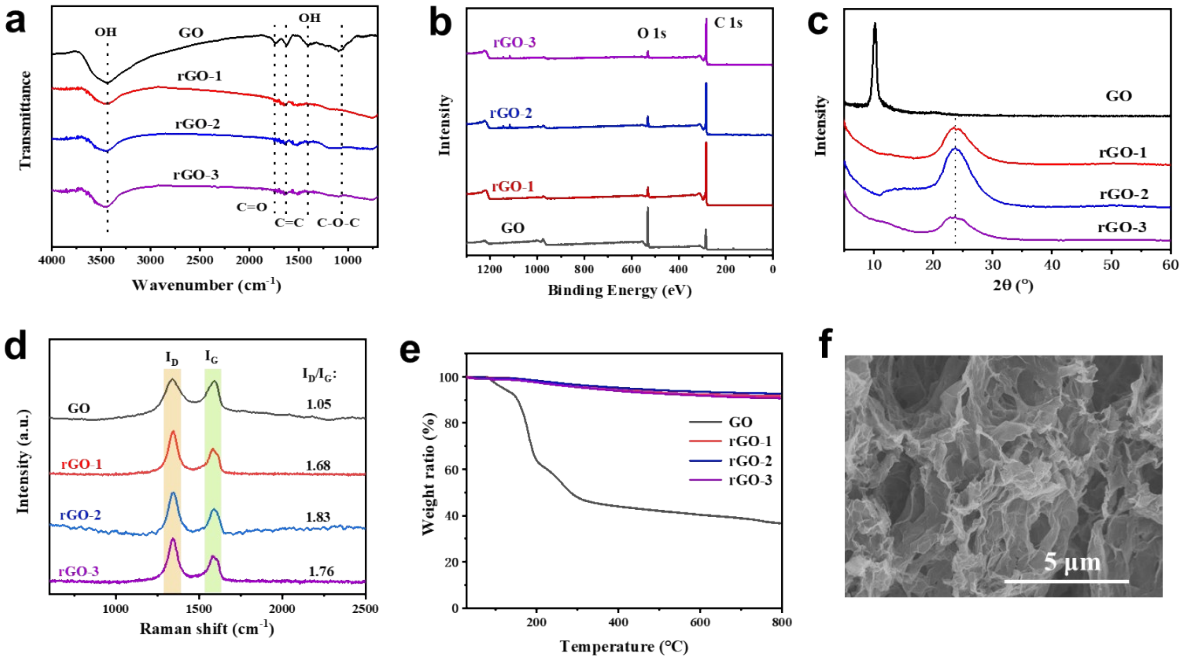

Fig. S3. Various characterizations of GO and rGO (rGO-1, rGO-2 and rGO-3) obtained via reduction using different ratios of LM: a) FTIR spectra, b) XPS spectra, c) XRD patterns, d) Raman spectra, e) TGA plots, and f) SEM image.

Discussion: GO Reduction with LMs

Based on the confirmation experiment, the reduction process is shown in **Fig. S2a**. First, LMs were added into a GO suspension under ultrasonication with the color of the suspension changing from brown into gray. After the introduction of HCl, the color of the GO suspension turned black within 30 min; moreover, after further addition of HCl, rGO was obtained by dissolving excessive LMs. As for the blend solution of LMs and GO, LM particles were coated with GO sheets. As shown in **Fig. S2b**, some clearly visible graphene sheets fold on the surface of the LM particles. **Fig. S2c** shows the elemental mapping of typical GO-coated LM particles. The presence of C and O across the Ga particles demonstrate that the LM particles are covered with GO. This coating phenomenon can be attributed to the interaction between LM and oxygen-containing functional groups, such as carboxyl and hydroxy.[2, 3] Microstructure images of various LMs/GO ratios (1:1, 2:1, and 3:1) are shown in **Fig. S2d**, and the resulting rGOs are denoted as rGO-1, rGO-2, and rGO-3. The resulting close contact between GO and LM

facilitates the reduction of GO due to the fast electron transport from Ga/Ga^{3+} to GO sheets. According to the previously reported studies, this reduction process can be expressed as follows: [4-6]

$$GO + H^+ + e^- \rightarrow rGO + H_2O$$

Due to the removal of large amounts of oxygen-containing functional groups of GO, the characteristic absorption bands of C–O–C, C–O, and C-OH from the FTIR spectrum exhibit a decrease in intensities after reduction of GO (**Fig. S3a**). Moreover, the C/O ratio of rGO remarkably increases from 1.78 to approximately 13 after GO reduction, according to the XPS spectra (**Fig. S3b**), indicating that LM is more effective than other similar reducing agents (**Table S1**). After reduction, the lattice structure of graphene also changed significantly. As shown in the XRD patterns, the diffraction peak of GO at approximately 10° is sharp; however, the obtained rGOs only exhibit broad diffraction peak from 20° to 30°, confirming the incomplete restoration of the graphite crystal structure (**Fig. S3c**). Similarly, the corresponding Raman spectra also present distinct changes. The intensity ratios (I_D/I_G) of D and G band of GO and rGO show a distinct change from 1.05 to more than 1.5 (**Fig. S3d**). The elimination of labile oxygen-containing functional groups is more directly reflected in TGA curves. After heat treatment, the final residual mass of GO is only 37 %, whereas that of rGO is up to 95% at 800 °C (**Fig. S3e**). Finally, the microstructure image reveals that the rGO material comprise randomly aggregated, thin, crumpled sheets closely associated with each other (**Fig. S3f**). Therefore, LMs can effectively reduce GO in acidic aqueous solutions, which provides the basis for the subsequent preparation of PAA-LM/rGO composite hydrogels.

Table S1. C/O atomic ratio of rGO at different studies

Green reducing agents	C/O atomic ratio	Ref.
Zn powder	2.3	5
Iron powder	7.9	6
Hydroxyl amine	9.7	7
L-Ascorbic acid	5.7	8
Metallic Mg	3.76	9
Glycine	11.14	10
Carrot root	11.9	11
Sodium carbonate	8.15	12
Ga-liquid metal	**13**	**This work**

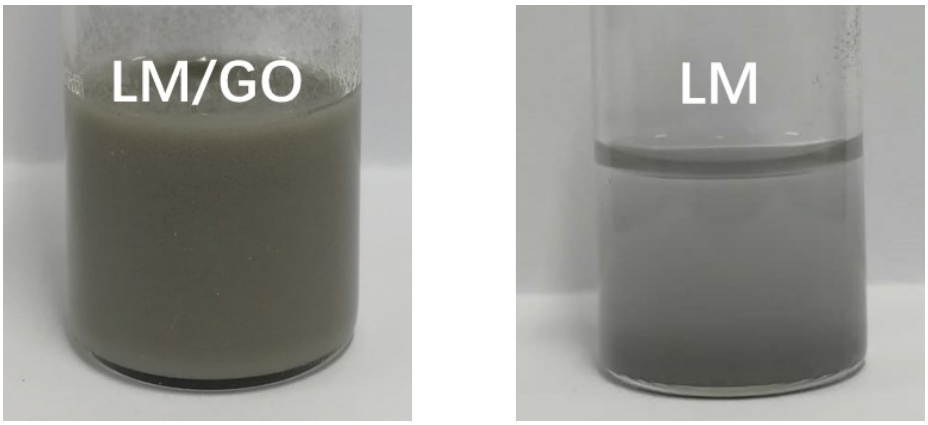

Fig. S4. The homogeneous and stable dispersion of LMs in water with the GO assistance, and the unstable dispersion of pure LMs in water (store for 30 minutes).

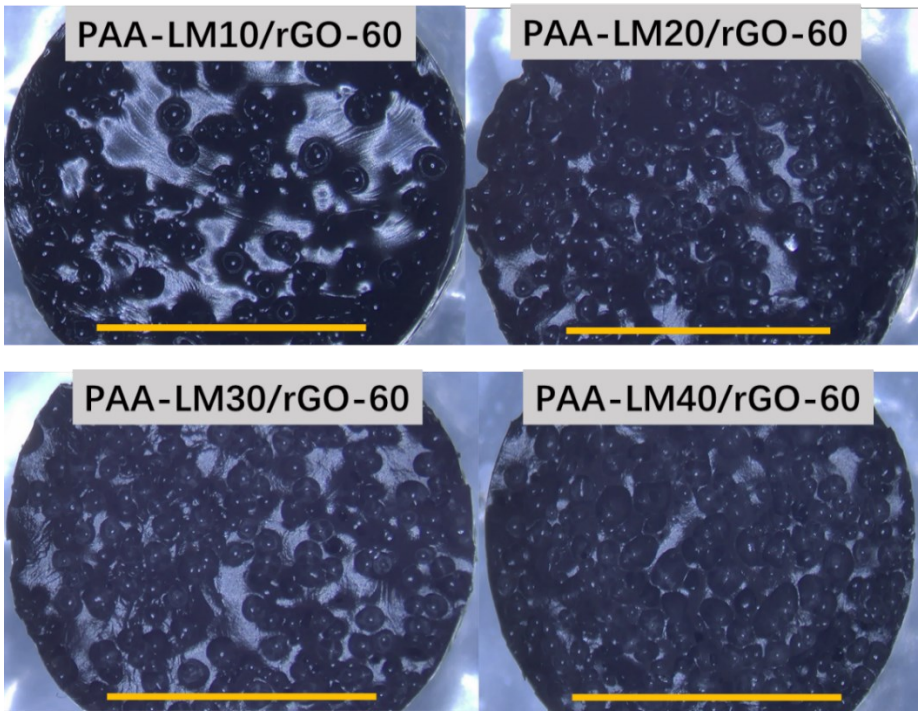

Fig. S5. Photos of the cross section of various PAA-LM/rGO hydrogels obtained at 60 °C (scale bar: 10 mm).

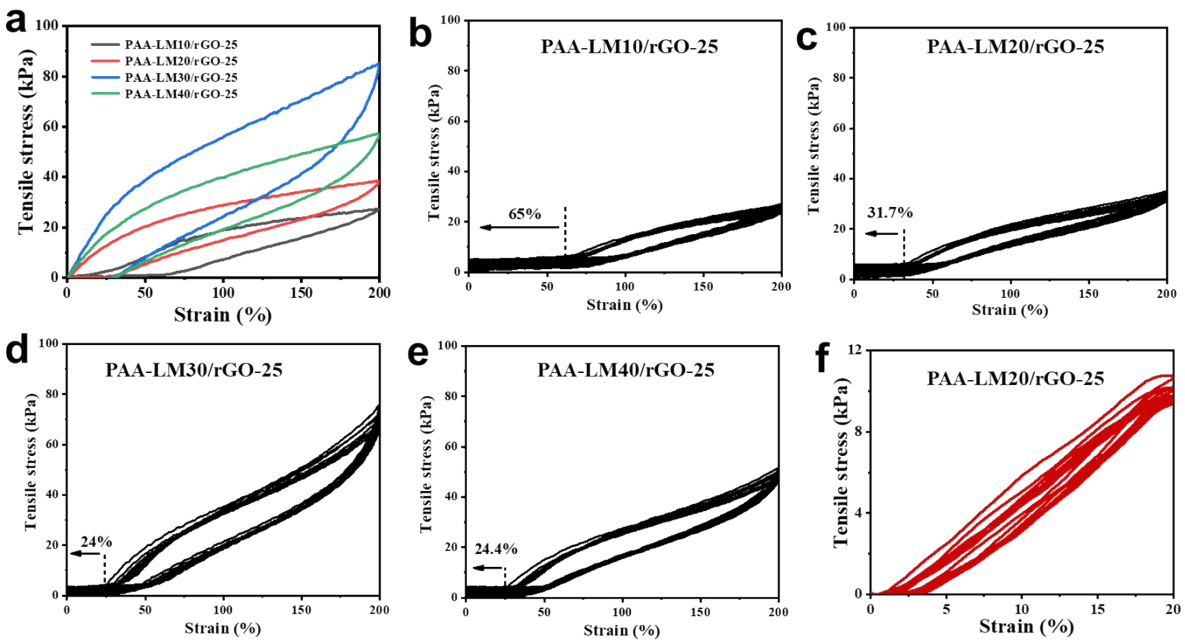

Fig. S6. a) The first loading-unloading cycles of all the hydrogels prepared at room temperature, and b-e) their following multiple loading-unloading cycles. f) Ten successive loading-unloading cycles of PAA-LM20/rGO-25 hydrogel at a small strain.

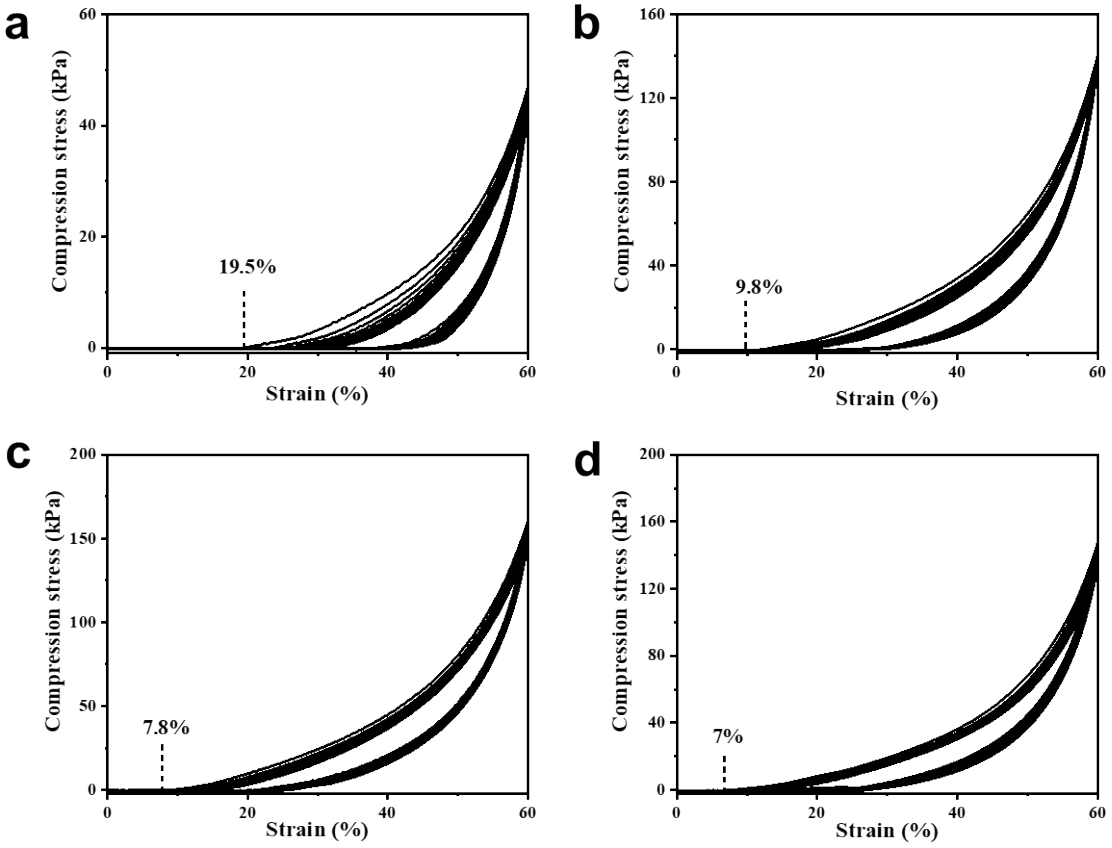

Fig. S7. The loading–unloading cycles (from second to ten cycle) of compressive test: a) PAA-LM10/rGO-25, b) PAA-LM20/rGO-25, c) PAA-LM30/rGO-25, d) PAA-LM40/rGO-25.

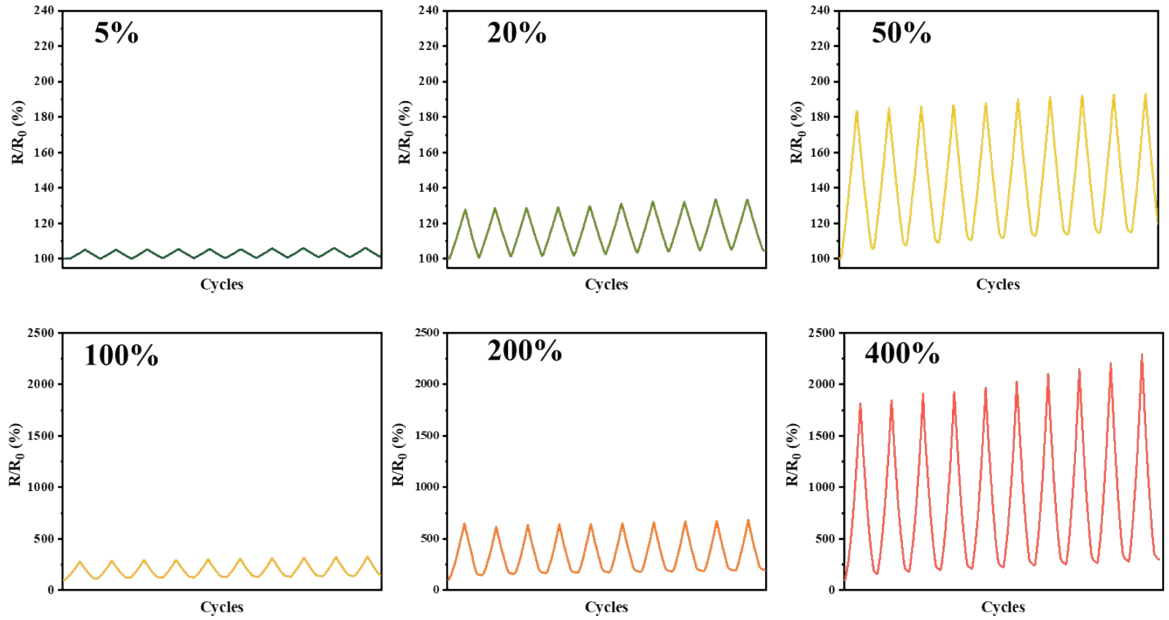

Fig. S8. Relative resistance changes in PAA-LM20/rGO-25 hydrogel during multiple stretching cycles under small strain (5%–50%) and large strain (100%–400%).

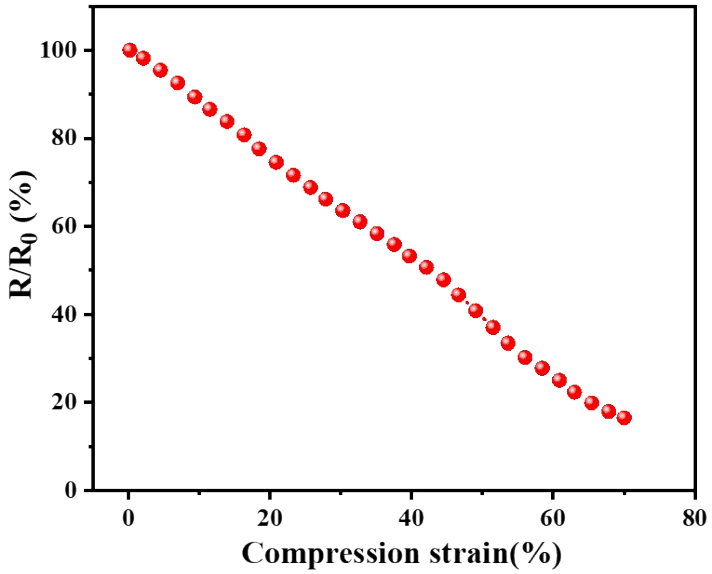

Fig. S9. Relative resistance changes of the PAA-LM20/rGO-25 hydrogel during large compression strain.

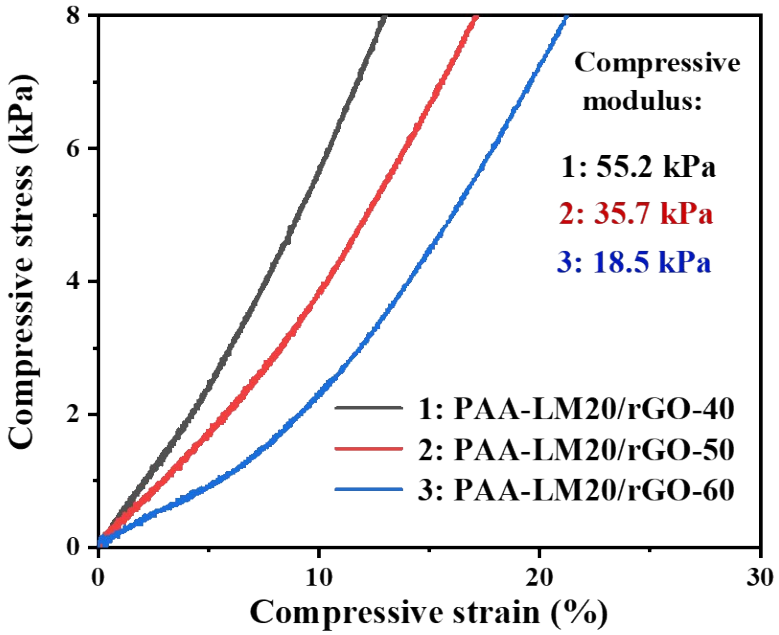

Fig. S10. The compression stress–strain curves of the PAA-LM20/rGO hydrogels in the strain ranges of 0-30%.

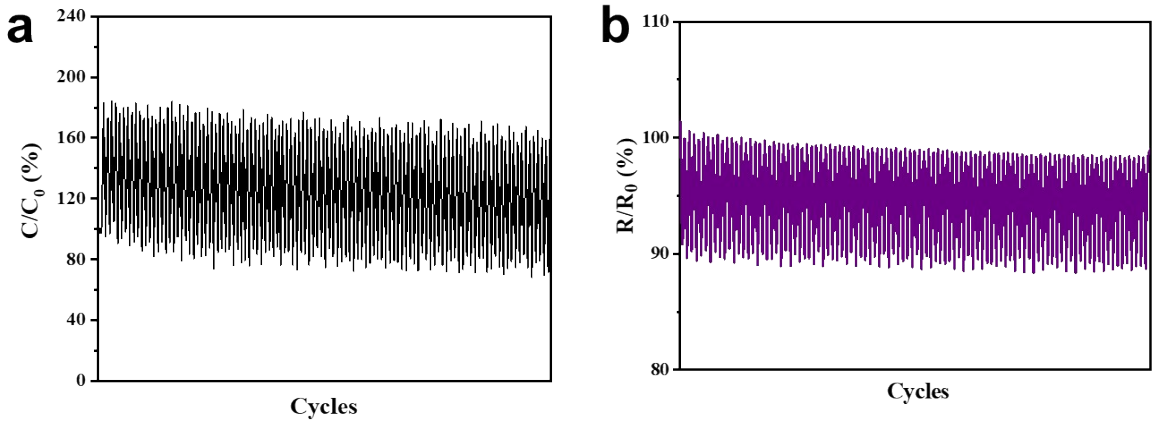

Fig. S11. Cycling compressive stability tests of the PAA-LM20/rGO-25 hydrogel to capacitance a) and resistance b) over 100 cycles.

Table S2. Summary of the recent hydrogel sensor or the similar sensor.

System	Tensile strain sensitivity (GF)	Compression stress sensitivity (/kPa)	Other sensations	Stretchability (%)	Self-healing ability	Ref.
PAM/PHEA-LM hydrogels	—	0.25	No	1500	No	13
PAA-LM hydrogels	1.54	—	No	1200	Yes	14
PAA/alginate-LM hydrogels	0.4	—	No	—	No	15
Polyionic elastomers	1	0.02	Temperature Humidity	100000	Yes	16
3D printed responsive hydrogels	—	0.45	Temperature	—	No	17
3D printed ionic conductors	—	0.84	No	650	No	18
Polyelectrolyte/ionic liquids elastomers	1	0.01	Temperature Humidity Solvent	100000	Yes	19
Polyurethane/ionic liquids	1.54	0.37	No	320	Yes	20
Porous structure sensor	—	0.63	No	—	Yes	21
PAM/PVA hydrogels	—	0.05	No	500	No	22
PAA/Ta@CNC hydrogels	4.9-8	—	No	2700	Yes	23
Microsphere structured hydrogels	—	0.35	No	600	No	24
PAA/rGO hydrogels	1.32	—	No	650	Yes	25
PAA-LM/rGO hydrogels	**1.77-9.86**	**0.16-0.85**	**Temperature Solvent Negative air pressure**	**675-2900**	**Yes**	**This work**

References

1. H. Yu, B. Zhang, C. Bulin, R. Li and R. Xing, *Sci. Rep.*, 2016, **6**, 36143.
2. T. Gan, W. Shang, S. Handschuh-Wang and X. Zhou, *Small*, 2019, **15**, 1804838;
3. X. Li, M. Li, L. Zong, X. Wu, J. You, P. Du and C. Li, *Adv. Funct. Mater.*, 2018, **28**, 1804197.
4. Y. Lin, C. Boyer, S. Zhu and D.-W. Wang, *ChemPlusChem*, 2018, **83**, 947-955;
5. Y. Liu, Y. Li, M. Zhong, Y. Yang, Y. Wen and M. Wang, *J. Mater. Chem.*, 2011, **21***,* 15449-15455;
6. Z.-J. Fan, W. Kai, J. Yan. T. Wei, L. -J. Zhi, J. Feng, Y. -M. Ren, L. -P. Song and F. Wei. *ACS nano*, 2011*,* **5**, 191-198.
7. X. Zhou, J. Zhang, H. Wu, H. Yang, J. Zhang and S. Guo, *J. Phys. Chem. C*, 2011, **115**, 11957-11961.
8. J. Zhang, H. Yang, G. Shen, P. Cheng, J. Zhang and S. Guo, *Chem. Commu.*, 2010, **46***,* 1112-1114.
9. M. Sohn, E. Park, B. M. Yoo, T. H. Han, H. B. Park and H. Kim, *Carbon*, 2016*,* **110**, 79-86.
10. S. Bose, T. Kuila, A. K. Mishra, N. H. Kim and J. H. Lee, *J. Mater. Chem.*, 2012, **22**, 9696-9703.
11. T. Kuila, S. Bose, P. Khanra, A. K. Mishra, N. H. Kim and J. H. Lee, *Carbon*, 2012, **50**, 914-921.
12. Y. Jin, S. Huang, M. Zhang, M. Jia and D. Hu, *Appl. Surf. Sci.*, 2013, **268**, 541-546.
13. H. Peng, Y. Xin, J. Xu, H. Liu and J. Zhang, *Mater. Horiz.*, 2019, **6**, 618-625.
14. J. Xu, Z. Wang, J. You, X. Li, M. Li, X. Wu and C. Li, *Chem. Eng. J.*, 2020, **392**, 123788.
15. H. Liu, M. Li, C. Ouyang, T. J. Lu, F. Li and F. Xu, *Small*, 2018, **14**, 1801711.
16. Z. Lei and P. Wu, *Mater. Horiz.*, 2019, **6**, 538-545.
17. Z. Y. Lei, Q. K. Wang and P. Y. Wu, *Mater. Horiz.*, 2017, **4**, 694-700.
18. X. Yin, Y. Zhang, X. Cai, Q. Guo, J. Yang and Z. Wang, *Mater. Horiz.*, 2019, **6**, 767-780.
19. Z. Lei and P. Wu, *Nat. Commun.*, 2019, **10**, 3429.
20. T. Li, Y. Wang, S. Li, X. Liu and J. Sun, *Adv. Mater.*, 2020, **32**, 2002706.
21. S. Kang, J. Lee, S. Lee, S. Kim, J.-K. Kim, H. Algadi, S. Al-Sayari, D.-E. Kim, D. Kim and T. Lee, *Adv. Funct. Mater.*, 2016, **2**, 1600356.
22. G. Ge, Y. Z. Zhang, J. J. Shao, W. J. Wang, W. L. Si, W. Huang and X. C. Dong, *Adv. Funct.Mater.*, 2018, **28**, 1802576.
23. C. Y. Shao, M. Wang, L. Meng, H. L. Chang, B. Wang, F. Xu, J. Wang and P. B. Wan, *Chem. Mater.*, 2018, **30**, 3110-3121.

24. J. Duan, X. Liang, J. Guo, K. Zhu and L. Zhang, *Adv. Mater.*, 2016, **28**, 8037-8044.
25. X. Jing, H. Y. Mi, X. F. Peng and L. S. Turng, *Carbon*, 2018, **136**, 63-72.